

CryoEM and AI reveal a structure of SARS-CoV-2 Nsp2, a multifunctional protein involved in key host processes

Kliment Verba (✉ kliment.verba@ucsf.edu)

University of California, San Francisco

Meghna Gupta

University of California, San Francisco

Caleigh Azumaya

University of California, San Francisco

Michelle Moritz

University of California, San Francisco

Sergei Pourmal

University of California, San Francisco

Amy Diallo

University of California, San Francisco

Gregory Merz

University of California, San Francisco

Gwendolyn Jang

University of California, San Francisco

Mehdi Bouhaddou

University of California, San Francisco

Andrea Fossati

University of California, San Francisco

Axel Brilot

University of California, San Francisco

Devan Diwanji

University of California, San Francisco

Evelyn Hernandez

University of California, San Francisco

Nadia Herrera

University of California, San Francisco

Huong Kratochvil

University of California, San Francisco

Victor Lam

University of California, San Francisco

Fei Li

University of California, San Francisco

Yang Li

University of California, San Francisco

Henry Nguyen

University of California, San Francisco <https://orcid.org/0000-0002-6142-8807>

Carlos Nowotny

University of California, San Francisco

Tristan Owens

University of California, San Francisco

Jessica Peters

University of California, San Francisco

Alexandrea Rizo

University of California, San Francisco <https://orcid.org/0000-0003-4813-6348>

Ursula Schulze-Gahmen

The J. David Gladstone Institutes

Amber Smith

University of California, San Francisco

Iris Young

University of California, San Francisco

Zanlin Yu

University of California, San Francisco

Daniel Asarnow

University of California, San Francisco

Christian Billesbølle

University of California, San Francisco

Melody Campbell

Fred Hutchinson Cancer Research Center <https://orcid.org/0000-0003-1909-5751>

Jen Chen

University of California, San Francisco

Kuei-Ho Chen

University of California, San Francisco

Un Seng Chio

University of California, San Francisco

Miles Dickinson

University of California, San Francisco <https://orcid.org/0000-0002-8016-1570>

Loan Doan

University of California, San Francisco

Mingliang Jin

University of California, San Francisco

Kate Kim

University of California, San Francisco

Junrui Li

University of California, San Francisco

Yen-Li Li

University of California, San Francisco

Edmond Linossi

The Walter and Eliza Hall Institute of Medical Research

Yanxin Liu

University of California, San Francisco <https://orcid.org/0000-0002-2253-3698>

Megan Lo

University of California, San Francisco

Jocelyne Lopez

University of California, San Francisco

Kyle Lopez

University of California, San Francisco

Adamo Mancino

University of California, San Francisco

Frank Moss III

University of California, San Francisco

Michael Paul

University of California, San Francisco

Komal Pawar

University of California, San Francisco

Adrian Pelin

University of California, San Francisco

Thomas Pospiech Jr.

University of California, San Francisco

Cristina Puchades

University of California, San Francisco

Soumya Remesh

University of California, San Francisco

Maliheh Safari

University of California, San Francisco

Kaitlin Schaefer

University of California, San Francisco

Ming Sun

Columbia University <https://orcid.org/0000-0002-4413-2502>

Mariano Tabios

University of California, San Francisco

Aye Thwin

University of California, San Francisco

Erron Titus

University of California, San Francisco <https://orcid.org/0000-0001-6868-9121>

Raphael Trenker

University of California, San Francisco

Eric Tse

University of California, San Francisco <https://orcid.org/0000-0002-2082-9006>

Tsz Kin Martin Tsui

University of California, San Francisco

Feng Feng

University of California, San Francisco

Kaihua Zhang

University of California, San Francisco

Yang Zhang

University of California, San Francisco

Jianhua Zhao

University of California, San Francisco

Fengbo Zhou

University of California, San Francisco

Yuan Zhou

University of California, San Francisco

Lorena Zuliani-Alvarez

University of California, San Francisco

David Agard

University of California, San Francisco <https://orcid.org/0000-0003-3512-695X>

Yifan Cheng

Howard Hughes Medical Institute <https://orcid.org/0000-0001-9535-0369>

James Fraser

University of California, San Francisco

Natalia Jura

University of California, San Francisco <https://orcid.org/0000-0001-5129-641X>

Tanja Kortemme

University of California, San Francisco <https://orcid.org/0000-0002-8494-680X>

Aashish Manglik

University of California, San Francisco <https://orcid.org/0000-0002-7173-3741>

Daniel Southworth

University of California, San Francisco <https://orcid.org/0000-0001-7108-9389>

Robert Stroud

University of California, San Francisco <https://orcid.org/0000-0003-2083-5665>

Danielle Swaney

University of California, San Francisco

Nevan Krogan

University of California, San Francisco <https://orcid.org/0000-0003-4902-337X>

Adam Frost

University of California, San Francisco <https://orcid.org/0000-0003-2231-2577>

Oren Rosenberg

University of California, San Francisco <https://orcid.org/0000-0002-5736-4388>

Article

Keywords: SARS-CoV-2, proteins, drug design

Posted Date: May 19th, 2021

DOI: <https://doi.org/10.21203/rs.3.rs-515215/v1>

License: © ⓘ This work is licensed under a Creative Commons Attribution 4.0 International License.

[Read Full License](#)

Title: CryoEM and AI reveal a structure of SARS-CoV-2 Nsp2, a multifunctional protein involved in key host processes.

Authors: Meghna Gupta^{1*}, Caleigh M. Azumaya^{1*}, Michelle Moritz^{1*}, Sergei Pourmal^{1*}, Amy Diallo^{1*}, Gregory E. Merz^{1*}, Gwendolyn Jang^{2,3,4,5*}, Mehdi Bouhaddou^{2,3,4,5*}, Andrea Fossati^{2,3,4,5*}, Axel F. Brilot¹, Devan Diwanji¹, Evelyn Hernandez¹, Nadia Herrera¹, Huong T. Kratochvil¹, Victor L. Lam¹, Fei Li¹, Yang Li¹, Henry C. Nguyen¹, Carlos Nowotny¹, Tristan W. Owens¹, Jessica K. Peters¹, Alexandria N. Rizo¹, Ursula Schulze-Gahmen¹, Amber M. Smith¹, Iris D. Young¹, Zanlin Yu¹, Daniel Asarnow¹, Christian Billesbølle¹, Melody G. Campbell^{1,6}, Jen Chen¹, Kuei-Ho Chen^{2,3,4,5}, Un Seng Chio¹, Miles Sasha Dickinson¹, Loan Doan¹, Mingliang Jin¹, Kate Kim¹, Junrui Li¹, Yen-Li Li¹, Edmond Linossi¹, Yanxin Liu¹, Megan Lo¹, Jocelyne Lopez¹, Kyle E. Lopez¹, Adamo Mancino¹, Frank R. Moss III¹, Michael D. Paul¹, Komal Ishwar Pawar¹, Adrian Pelin^{2,3,4,5}, Thomas H. Pospiech Jr.¹, Cristina Puchades¹, Soumya Govinda Remesh¹, Maliheh Safari¹, Kaitlin Schaefer¹, Ming Sun^{1,7}, Mariano C Tabios¹, Aye C. Thwin¹, Erron W. Titus¹, Raphael Trenker¹, Eric Tse¹, Tsz Kin Martin Tsui¹, Feng Wang¹, Kaihua Zhang¹, Yang Zhang¹, Jianhua Zhao¹, Fengbo Zhou¹, Yuan Zhou^{2,3,4,5}, Lorena Zuliani-Alvarez^{1,2,3,4,5}, QCRG Structural Biology Consortium¹, David A Agard^{1,2,3,8}, Yifan Cheng^{1,2,3,8,9}, James S Fraser^{1,2,3,8}, Natalia Jura^{1,2,3,11}, Tanja Kortemme^{1,2,3,10,12}, Aashish Manglik^{1,2,3,13}, Daniel R. Southworth^{1,2,3,8}, Robert M Stroud^{1,2,3,8}, Danielle L Swaney^{2,3,4,5}, Nevan J Krogan^{2,3,4,5,16,&}, Adam Frost^{1,2,3,8,14,&}, Oren S Rosenberg^{1,2,3,8,14,15,&}, Kliment A Verba^{1,2,3,13,&}

Affiliations

¹QBI Coronavirus Research Group Structural Biology Consortium, University of California, San Francisco, CA 94158, USA.

²Quantitative Biosciences Institute (QBI) COVID-19 Research Group (QCRG), San Francisco, CA 94158, USA.

³QBI, University of California, San Francisco, CA 94158, USA.

⁴Department of Cellular and Molecular Pharmacology, University of California, San Francisco, CA 94158, USA.

⁵J. David Gladstone Institutes, San Francisco, CA 94158, USA.

⁶Current affiliation: Division of Basic Sciences, Fred Hutchinson Cancer Research Center, Seattle, WA 98109, USA.

⁷Current affiliation: Beam Therapeutics, Cambridge, MA 02139, USA

⁸Department of Biochemistry and Biophysics, University of California, San Francisco, CA 94158, USA.

⁹Howard Hughes Medical Institute, San Francisco, CA 94158, USA.

¹⁰Department of Bioengineering and Therapeutic Sciences, University of California, San Francisco, CA 94158, USA.

¹¹Cardiovascular Research Institute, University of California, San Francisco, CA 94158, USA.

¹²The University of California, Berkeley–University of California, San Francisco Graduate Program in Bioengineering, University of California, San Francisco, CA 94158, USA.

¹³Department of Pharmaceutical Chemistry, University of California, San Francisco, CA 94158, USA.

¹⁴Chan-Zuckerberg Biohub, San Francisco, CA 94158, USA.

¹⁵Department of Medicine, University of California, San Francisco, CA 94143, USA.

¹⁶Department of Microbiology, Icahn School of Medicine at Mount Sinai, New York, NY 10029, USA.

* These authors contributed equally to this work.

& Corresponding authors. A.F., O.S.R. and K.A.V. are corresponding authors on behalf of QCRG Structural Biology Consortium

52 **Abstract**

53 The SARS-CoV-2 protein Nsp2 has been implicated in a wide range of viral processes, but its
54 exact functions, and the structural basis of those functions, remain unknown. Here, we report an
55 atomic model for full-length Nsp2 obtained by combining cryo-electron microscopy with deep
56 learning-based structure prediction from AlphaFold2. The resulting structure reveals a
57 highly-conserved zinc ion-binding site, suggesting a role for Nsp2 in RNA binding. Mapping
58 emerging mutations from variants of SARS-CoV-2 on the resulting structure shows potential
59 host-Nsp2 interaction regions. Using structural analysis together with affinity tagged purification
60 mass spectrometry experiments, we identify Nsp2 mutants that are unable to interact with the
61 actin-nucleation-promoting WASH protein complex or with GIGYF2, an inhibitor of translation
62 initiation and modulator of ribosome-associated quality control. Our work suggests a potential
63 role of Nsp2 in linking viral transcription within the viral replication-transcription complexes
64 (RTC) to the translation initiation of the viral message. Collectively, the structure reported here,
65 combined with mutant interaction mapping, provides a foundation for functional studies of this
66 evolutionary conserved coronavirus protein and may assist future drug design.

67

68 **Introduction**

69 Upon entry into human cells SARS-CoV-2, the causative agent of COVID-19, produces
70 two large polyproteins, pp1a and pp1ab. These polyproteins are further processed by two viral
71 proteases into 16 individual non-structural proteins (nsp1-nsp16). These non-structural proteins
72 fulfill a number of essential viral functions including RNA replication, replication proofreading,
73 double-membrane vesicle formation, and others¹. Many of these also interact with host factors
74 to effectively subvert the host cell to meet the virus's needs². Such subversion, for example,
75 includes suppressing host innate immune responses, host translation, nuclear import, and other
76 effects³⁻⁵. Despite their central importance to viral pathogenesis, many non-structural proteins
77 remain structurally and functionally uncharacterized. Furthermore, the interactions between

78 virus and host proteins are even less understood, with only a handful of unique viral-host protein
79 complex structures available. As viruses often hijack central nodes in host cell pathways,
80 studying viral-host interactions in molecular detail can lead to a better understanding of the
81 mechanisms of viral pathogenesis and of the fundamental host cell processes the virus targets.
82 In addition, viral-host protein complexes are an attractive target for antiviral therapeutics as they
83 are less likely to accrue resistance. In this report we focus on one of the least studied
84 SARS-CoV-2 proteins, Nsp2.

85 Neither the functions nor the structure of Nsp2 are known. In SARS-CoV-1, Nsp2
86 deletion leads to a defect in viral replication but still yields viable viruses⁶. Interestingly,
87 expression of Nsp2 from an alternate site in the genome does not rescue this defect, likely
88 indicating the importance of correct timing for Nsp2 expression⁷. A number of studies mapping
89 host-viral interactomes of SARS-CoV-1/2 and MERS have identified host proteins that interact
90 with Nsp2⁸⁻¹¹. These studies have implicated Nsp2 in processes ranging from translation
91 repression to endosomal transport, ribosome biogenesis, and actin filament binding. Nsp2 in
92 SARS-CoV-2 and other coronaviruses have been observed to localize to endosomes and
93 replication-transcription complexes (RTC); but it's currently unclear what role Nsp2 plays at
94 these sites^{10,12}. Although Nsp2 is present in SARS-CoV-1, CoV-2, MERS—and in closely related
95 coronaviruses in bats, pangolins and other animals—there is a considerable sequence variation
96 across different species (Sup Fig 1). This degree of variability may indicate rapid Nsp2
97 adaptation under host-specific selection pressures. Furthermore, genome sequencing of
98 SARS-CoV-2 variants during the COVID19 pandemic reveals sites under positive selection in
99 Nsp2, suggesting host-specific human adaptation following successful zoonotic transfer¹³.
100 Importantly, a specific mutation in Nsp2, T85I, is observed in clade 20C (as per Nexstrain
101 nomenclature) including both variants of interest (B.1.526) and variants of concern
102 (B.1.427/B.1.429 recently identified in California)^{14,15}. Genetic knockdown/knockout studies have

103 shown that a number of Nsp2 host interactors negatively affect SARS-CoV-2 replication, further
104 corroborating the functional importance of Nsp2^{10,16}.

105 Structural models of Nsp2 and Nsp2-host protein complexes will allow spatial mapping
106 of the growing list of mutations and potentially shine light on their significance for Nsp2
107 functions. By delineating which Nsp2 surfaces determine specific Nsp2-host protein interactions,
108 researchers will be able to generate specific Nsp2 point mutants that are defective in forming
109 these protein complexes—helping tease apart the biological role of a particular Nsp2-host
110 interaction. However, there are neither structures available for Nsp2 from any of the beta
111 coronaviruses family members nor are there any similar structures in the PDB based on the
112 sequence homology. Here we present a structure of SARS-CoV-2 Nsp2 derived from a
113 combination of cryo-EM experimental data and AlphaFold2 prediction. Utilizing the natural
114 sequence variation in SARS-CoV-2 together with our structure and mass spectrometry
115 experiments, we identify two key Nsp2 surfaces that are required for specific host interactions.

116

117 **Results**

118

119 **Combining a cryo-EM map with AlphaFold2 Nsp2 predictions yields a pseudo-atomic** 120 **structure for full-length Nsp2**

121 Full-length SARS-CoV-2 Nsp2 was recombinantly expressed and purified from *E.coli*
122 cells. After purification involving multiple steps to remove contaminating nucleic acids, Nsp2 was
123 obtained at high purity, plunge frozen, and imaged by cryo-electron microscopy. Processing in
124 cryoSPARC2^{17,18} followed by RELION3¹⁹ yielded a reconstruction of Nsp2 at 3.8 Å global
125 resolution ranging from 3Å in the best resolved regions to 6Å in the most flexible regions (Fig 1A
126 and Sup Fig 2). The initial model was automatically built into the well-resolved region using the
127 DeepTracer^{20,21} online server and then further corrected and refined via manual manipulation in
128 Coot²² and ISOLDE²³, followed by final refinements in Phenix²⁴ and Rosetta²⁵ (see methods).

129 Having built an initial model, we then identified a number of putative zinc binding sites and
130 repeated the sample purification and cryo-EM imaging in the presence of zinc. This yielded an
131 improved 3.2 Å cryo-EM map, which revealed additional details and enabled improved modeling
132 of residues 5-505 of the SARS-CoV-2 Nsp2 (Fig 1B). To our surprise, under these Zn-included
133 conditions the density for the C-terminal 130 amino acids was completely missing. In the
134 cryo-EM map without zinc, although the density for the flexible C-terminal domain was present,
135 it was resolved at between 5-6 Å resolution. The closest homologous structure showed less
136 than 10% sequence identity (PDB:3LD1)²⁶, and as the domain was predicted to be high in the
137 beta sheet fold this posed a significant challenge for *de novo* modeling based on low-resolution
138 cryo-EM density alone.

139 The recent utilization of deep learning for protein structure prediction based on amino
140 acid sequence has led to a new level of success, as demonstrated by CASP14²⁷. Specifically,
141 the AlphaFold2 team was able to predict protein structures with unprecedented accuracy,
142 producing results sometimes indistinguishable from the experimentally derived structures.
143 AlphaFold2 and other teams in the CASP14 also ran predictions on SARS-CoV-2 proteins,
144 including Nsp2. Out of all the available predicted models for Nsp2, only one model has an
145 RMSD of less than 20 Å to our experimental model: C1901TS156_4 from the AlphaFold2 team.
146 The other 5 models from AlphaFold2 were also close to 20Å RMSD, so we aligned all the
147 available Nsp2 models from the AlphaFold2 team (5 from the CASP14 and one updated model
148 available on their website²⁸) to our structure (Sup Fig 3). This comparison made it clear that,
149 globally, the predictions were quite different from the experimentally derived structure. In
150 addition, the most updated model was missing a prediction for 93 amino acids of the protein (Fig
151 1C).

152 However, when analyzed in isolation, the individual motifs and domains of the proteins
153 are remarkably close to the experimentally derived structure. This observation prompted us to
154 break the model down into 4 subregions and align them to the experimentally derived structure

155 independently. This yielded high local similarity per domain (average RMSD values of less than
156 2 Å, Fig 1D). The prediction for the missing C-terminal 130 amino acids in isolation fit well within
157 the lower resolution density for that domain in the cryoEM map without zinc. We therefore
158 combined the AlphaFold2 domain prediction for the C-terminal 130 amino acids with our
159 experimentally built cryo-EM model to yield an experimentally valid and complete structure of
160 full-length Nsp2 (Fig 1E, Sup Table 1).

161

162 **Nsp2 shows low global conservation among beta-coronaviruses, but possesses a highly**
163 **conserved Zn binding motif.**

164 To better understand which regions of Nsp2 are functionally important, we performed a
165 sequence alignment of Nsp2 across beta-coronaviruses from different species. Nsp2 shows low
166 conservation, with the N-terminal half of the protein being marginally more conserved (Fig 2A
167 and Sup Fig 1). Overall, SARS-CoV-2 Nsp2 is 68% identical to SARS-CoV-1 Nsp2 and only
168 20% identical to MERS virus Nsp2. Strikingly, the most conserved residues are a cysteine quad
169 coordinating a Zn²⁺ ion in a Zn ribbon like motif, with three of the four cysteines being invariant
170 across all the virus sequences. Performing a structural similarity search with this motif from
171 Nsp2 indicates that it is similar to zinc ribbons²⁹ in a number of RNA binding proteins in RNA
172 polymerases and ribosomes (Fig 2A insert, average RMSD for the region of 1.7 Å). In some of
173 these proteins these motifs explicitly have been implicated in RNA binding and in one structure
174 (PDB:1JJ2, chain 2), the zinc ribbon on the ribosomal protein L44E is directly interacting with
175 the ribosomal RNA. This motif is also similar to the tudor domains in the histone tail binding
176 protein JMJD2A (RMSD of 1.7 Å). Although the fold is similar, the tudor domain is missing a
177 Zn²⁺ ion in the JMJD2A structure (PDB:2QQS). Previous studies have associated Nsp2 with the
178 viral RTCs^{12,30} and during the purification from bacteria we observed strong, apparently
179 non-specific binding to *E.coli* nucleic acids that required chromatographic separation. One
180 possibility, therefore, is that this motif is important for Nsp2 interactions with nucleic acids.

181 In addition to the proteins containing zinc ribbons and tudor motifs, a search of the PDB
182 for structurally similar proteins returned only one additional structure, the structure of Nsp2 from
183 Avian Infectious Bronchitis virus (PDB:3LD1). Although the sequence identity is below 10% for
184 these proteins, the beta sheet C-terminal domain aligns well with our model. No other structures
185 came up in our structural similarity search with either the FATCAT³¹ or DALI ³²servers.

186

187 **Subsets of acquired mutations in Nsp2 group into surface patches.**

188 Examining the mutations that occur in SARS-CoV-2 Nsp2 during the COVID19
189 pandemic, over 50 sites have been identified as being under positive selection (at the time of
190 writing, based on the $dn/ds > 1$ metric^{33,13}). Most of these mutations occur at low frequency. Two
191 mutations however, T85I and I120F, are present at frequencies of roughly 13% and 5%
192 respectively. The T85I mutation maps to a surface residue on our structure (Fig 3). The side
193 chain of T85 is surface exposed, therefore replacing it with a hydrophobic isoleucine should not
194 be favorable. However, if this region of Nsp2 is involved in protein-protein interactions such a
195 substitution might be a gain-of-function change, stabilizing a hydrophobic binding interface. The
196 second residue that is mutated, I120F, is not surface exposed and instead packs in a
197 hydrophobic core that anchors a small helix. This small helix is attached to a highly charged
198 loop on the surface of the protein and its dynamics may be functionally important. A
199 phenylalanine mutation may further stabilize this helix anchor point by participating in
200 pi-stacking interactions with neighboring aromatic residues (Fig 3 inset).

201 The structure allowed us to map the spatial relationships of conserved residues in Nsp2
202 among SARS-CoV-2 strains, revealing unexpected regions of conservation and selection. To
203 identify rapidly evolving regions of the protein, we mapped all the positively-selected mutations
204 to the protein surface (Fig 4). This analysis revealed charged surfaces which are devoid of
205 mutations, potentially indicating surfaces important for conserved interactions (Fig 4). There are
206 also two residue clusters where mutations found in strain variants are proximal to one another

207 and alter the characteristics of the protein's surface in similar ways. Cluster 1 is near the
208 N-terminus consisting of three arginine residues (R27C, R52C, R4C) that mutate individually to
209 cysteines, reducing the exposed positive surface charge in that region and introducing a
210 sulfhydryl. Cluster 2 consists of six proximal residues which mutate individually to more
211 hydrophobic residues (G262V, G265V, G285V, A411V, T371I) (Fig 4) in the variant strains. In
212 both clusters, only individual single residue mutations are picked up in the viral population but
213 the fact that they form physical clusters and have similar biochemical consequences might
214 indicate adaptation.

215

216 **Affinity purification mass spectrometry identifies Nsp2 surfaces mediating specific host**
217 **interactions.**

218 To investigate whether common strain variants as well as disruptions of conserved
219 patches would affect Nsp2's ability to interact with host proteins we generated appropriate Nsp2
220 mutants and assessed changes in virus-human protein-protein interactions by affinity
221 purification mass spectrometry (AP-MS) in HEK293T cells². Three Nsp2 mutants were based on
222 the natural Nsp2 variations: T85I, D23Y/R27C (cluster 1), G262V/G265V (cluster 2) and two
223 were designed to disrupt the conserved/charged surface patches: K330D/K337D and
224 E63K/E66K. All mutants expressed at similar levels in HEK293T cells (Sup Fig 4). We began by
225 performing a global and unbiased quantification of virus-host protein-protein interactions using
226 an automated affinity purification mass spectrometry workflow (see Methods). T85I and
227 D23Y/R27C did not show significant changes in their interactomes, but three mutants did show
228 significant changes in host interactions: G262V/G265V mutations abrogated Nsp2 interactions
229 with the complex comprising GIGYF2/EIF4E2/RNF598³⁴, E63K/E66K reduced interactions
230 between Nsp2 and WASHC4/WASHC5 complex and also FKBP15, and K330D/K337D had a
231 severely reduced interaction with NADPH cytochrome P450 reductase (POR gene) (Figure
232 5A,B,D, Table S2). Interestingly, Nsp2 E63K/E66K also gained a large number of new

233 interactors which are predominantly involved in ribosomal RNA metabolic processes (Sup Fig
234 5). To increase the sensitivity and robustness of our quantitation, we performed Parallel
235 Reaction Monitoring (PRM) on the subset of significantly changed interactors from the Data
236 Dependent Analysis (DDA). Overall the PRM analysis recapitulated the findings of the DDA
237 (Figure 5C).

238

239 **Discussion**

240 In this report, we were able to combine cryoEM with recent advances in de novo protein
241 predictions to obtain a complete atomic model for SARS-CoV-2 Nsp2 protein. Although there
242 was a recent report of using AlphaFold2 predicted protein structure of Orf8 to solve the phase
243 problem in crystallographic studies, to our knowledge this is the first explicit use of AlphaFold2
244 predictions with restraints from an experimental cryoEM density for model building³⁵. This
245 exercise suggests that domain structure predictions from deep neural networks are increasingly
246 likely to be locally accurate and, when combined with experimental restraints, sufficient for
247 global structure prediction and integrative structural modelling. Electron cryo-microscopy and
248 cryo-tomography will be important sources of such overall shape information, and readily
249 obtainable, low-resolution measurements like negative stain electron microscopy, small-angle
250 X-ray scattering, cross-linking mass spectrometry, or even biochemical experiments may
251 provide sufficient constraints for accurate, global models to be determined in combination with
252 predicted domain structures. It is possible that further improvements in the prediction algorithms
253 will eliminate the need for experimental measurements entirely. However, atomic resolution
254 structures of multi-component and multi-domain assemblies are still relatively uncommon, and
255 this deficit of appropriate training data in the PDB may limit the accuracy of computational
256 models for multi-domain assemblies and higher-order complexes. Put another way, the
257 deficiency of data about protein-protein interfaces may mean that de-novo predictions of
258 complex assemblies will remain underdetermined for some time. Future work will explore the

259 use of restraints from 3D cryo-EM maps, 2D images, tomograms, and other data sources like
260 SAXS for the potential functions utilized by neural nets.

261 Our Nsp2 structure together with analysis of natural and designed sequence variation in
262 the Nsp2 of SARS-CoV-2 suggests a number of biological roles for Nsp2 and also regions of
263 interest on the protein. We identify a highly conserved zinc ribbon motif which structurally is
264 highly similar to zinc ribbons in RNA binding proteins. One possibility, therefore, is that this motif
265 is important for Nsp2 interactions with nucleic acids. Interestingly our mass spectrometry studies
266 on the E63K/E66K mutant, designed to introduce a charge reversal mutation in a conserved
267 negatively charged surface patch (Figs 4,5 and Sup Fig 5), show that this mutant gains a large
268 number of partners involved in ribosome biogenesis. Concurrently with this gain, this mutant
269 loses interactions with the endosomal/actin machinery (FKBP15, WASHC proteins^{36,37}). It is
270 tempting to speculate that Nsp2 binds ribosomal RNA (via the identified zinc ribbon) but
271 attachment to cytoskeletal elements at endosomes limits its interactions with rRNA. Upon
272 disruption of the endosomal anchoring of Nsp2 by the above mutations, Nsp2 is free to interact
273 with ribosomal RNAs—potentially even translocating to the nucleolus. Interestingly, previous
274 proximity labeling studies on murine coronavirus Nsp2 have uncovered an exciting link between
275 the viral polymerase within RTCs and the host cell's translation machinery¹². Since Nsp2 has
276 affinity for ribosomal RNA and is localized to RTCs, one appealing model is that Nsp2 plays a
277 role in locally enriching ribosomes next to viral messages for more efficient
278 transcriptional-translational coupling in the cytosol. Another aspect of these specific interactions
279 are potential roles that Nsp2 may play in hijacking the endosomal pathway to meet viral needs.
280 WASH complexes have been shown to play key roles in exocytosis and endosome biogenesis,
281 including cargo sorting through local Arp2/3 complex activation³⁸. SARS-CoV-2 enters cells
282 through the endosomal pathway and it may be functionally important for the virus to modulate
283 endosome pathways for successful infection.

284 Mass spectrometry analysis of the second Nsp2 mutant, G262V/G265V implicates Nsp2
285 in modulating ribosome-associated quality control. This mutant is based on the natural variants
286 of Nsp2 in the patch that is becoming more hydrophobic during the 2019-2020 COVID19
287 pandemic (Figure 4, cluster 2), although the natural variants all have a single mutation, either
288 the G262V or G265V. This mutant is the only one that specifically loses interactions with
289 GIGYF2, EIF4E2 and RNF598. These three proteins are known to form a complex and have
290 been implicated in inhibiting translation initiation when ribosomes stall on defective or abnormal
291 mRNA messages³⁴. At the moment it is unclear what is the exact functional connection between
292 SARS-CoV-2 infection and this recently discovered component of ribosome-associated quality
293 control mediated by GIGYF2/EIF4E2. Given that SARS-CoV-2 has optimized codon usage for
294 the human host, it is unlikely that there is increased ribosomal stalling on the viral message that
295 requires inhibition of GIGYF2/EIF4E2 by Nsp2^{39,40}. Furthermore, genetic studies have shown
296 that GIGYF2 and EIF4E2 are necessary rather than inhibitory for viral replication¹⁶. Perhaps the
297 virus uses Nsp2 to inhibit translation initiation of *host* messages, freeing ribosomes and the rest
298 of the translation machinery for virus production. Indeed, a prior study of the
299 GIGYF2/EIF4E2/ZNF598 complex suggests that in addition to its role in RQC, this complex
300 selectively suppresses transcripts involved in host inflammatory signaling, including IL-8⁴¹. It is
301 worth noting that Nsp2 interactions with GIGYF2/EIF4E2/ZNF598 complex is conserved across
302 SARS-CoV-1 and MERS indicating that this interaction might be of therapeutic importance for
303 coronaviruses generally¹⁰.

304 Our mass spectrometry experiments of the most prevalent Nsp2 mutation, T85I, did not
305 identify any changes in host interactions of this mutant. This may be due to our experiments
306 lacking the context of other viral proteins that would be present in a bona fide infection or
307 potentially due to the wrong cellular context. Alternatively this may suggest that some mutations
308 do not confer any fitness benefit and are simply present due to the C-U hypermutation observed
309 in SARS-CoV-2, which is likely driven by host mediated APOBEC editing⁴². Interestingly, there is

310 a recent report demonstrating that the SARS-CoV-2 Nsp2 T85I mutant shows a minor
311 replication defect in Vero green monkey cells, but has no effect in human cells. This is
312 consistent with the T85I mutation not conferring a strong selective advantage⁴³. Globally, the
313 second most prevalent SARS-CoV-2 amino acid substitution that is driven by the C-U
314 hypermutation is a T to I change. Therefore the T85I mutation in the 20C clade of SARS-CoV-2
315 may be neutral in fitness, but stable due to host-mediated RNA editing.

316 Overall, analysis of the resulting Nsp2 structure revealed a rapidly evolving protein
317 surface, with potential consequences for host-virus interactions. Leveraging the new structure
318 with natural Nsp2 variations and mass spectrometry we were able to identify surfaces important
319 for specific Nsp2 interactions. The pattern of disruption of interactions points to at least three
320 specific areas of biology that Nsp2 is involved in: interactions with endosomes through
321 cytoskeletal elements, interactions with modulators of translation, and also direct interactions
322 with ribosomal RNA. The exact roles Nsp2 plays in these pathways will require further
323 experimental characterization using the structure-based point mutants described here.

324

325

326 **Methods**

327 **Nsp2 Expression**

328 SARS-CoV-2 Nsp2, codon optimized for *Escherichia coli* expression, was cloned in a
329 pET-29b(+) vector backbone with N-terminus 10XHis-tag and SUMO-tag (Ep156). For
330 expression, the plasmid Ep156 was transformed in the LOBSTR *E. coli* strain and a single
331 colony was inoculated in LB media with 50 µg/ml kanamycin overnight at 37°C. 1% overnight
332 culture was inoculated in 1 L TB media with 50 µg/ml kanamycin and and grown at 37°C till
333 O.D._{600nm} reached 0.8. The culture was transferred to 20°C and induced with 0.5 mM IPTG for
334 16 h. The cells were harvested and washed with PBS, flash-frozen and stored at -80°C.

335

336 **Nsp2 Purification**

337 To a 6 L equivalent of cell pellet, 150 mL of lysis buffer (50 mM HEPES pH 7.5, 300 mM NaCl,
338 10% glycerol, 2 mM MgCl_2) supplemented with 2 protease inhibitor tablets (Roche), 1 mM
339 PMSF, and 30 μL benzonase nuclease (Millipore Sigma) was added. Cells were resuspended
340 and dounce homogenized before either sonication (3 x 10 min cycles using a sonifier (Branson),
341 at 50% duty cycle (1 sec on, 1 sec off), followed by ≥ 5 mins on ice, or high pressure
342 homogenizer (3 times passage through the EmulsiFlex-C3 [Avestin] at $\sim 15,000$ psi, 4°C). After
343 centrifugation for 40 mins at $25,000\times g$, 4°C , clarified samples were transferred to a 50 mL
344 conical tube and supplemented with a final 20 mM imidazole pH 7.5 before batch-binding with
345 Ni-NTA superflow resin (Qiagen) for ~ 1 hr at 4°C . The resins were collected in a gravity flow
346 column, washed with 15 CV lysis buffer, followed by 2x 7.5 CV sulfate wash buffer (25 mM Tris
347 pH 8.5, 300 mM NaCl, 10% glycerol, 100 mM Na_2SO_4), 2x 7.5 CV wash buffer (25 mM Tris pH
348 8.5, 300 mM NaCl, 10% glycerol, 30 mM imidazole), 2x 7.5 CV wash buffer supplemented with
349 2 mM ATP, 4 mM MgCl_2 , and eluted in 2x 2.5 CV elution buffer (25 mM Tris pH 8.0, 300 mM
350 NaCl, 10% glycerol, 300 mM imidazole, 2 mM MgCl_2). The elution was treated with benzonase
351 and Ulp1 protease and dialyzed overnight at 4°C in dialysis buffer (25 mM Tris pH 8.5, 75 mM
352 NaCl, 10% glycerol, 0.5 mM TCEP, 2 mM MgCl_2). The tagless Nsp2 was further purified using a
353 5 mL HiTrap Heparin HP column (Cytiva) using a linear gradient of 7.5% Heparin buffer A (30
354 mM Tris pH 8, 1 mM DTT) to 50% Heparin buffer B (30 mM Tris pH 8, 1 M NaCl, 1 mM DTT).
355 Peak fractions corresponding to Nsp2 were concentrated and further purified using a Superdex
356 200 increase 10/300 GL column (Cytiva) in SEC buffer (20 mM Tris pH 8.0, 250 mM NaCl, 0.5
357 mM TCEP) to yield a single peak. The peak fractions were pooled and concentrated and used
358 for CryoEM. For the Zn containing sample, 10 μM ZnCl_2 was kept in all the buffers of the
359 purification protocol mentioned above.

360

361 **CryoEM grid freezing and data collection**

362 Purified nsp2 was diluted to 6 μM for the apo sample and 5.7 μM for the Zn containing sample.
363 400 mesh 1.2/1.3R Au Quantifoil grids were glow discharged at 15 mA for 30 seconds.
364 Vitrification was done using FEI Vitrobot Mark IV (ThermoFisher) set up at 4°C and 100%
365 humidity. 3.5 μl sample was applied to the grids and the blotting was performed with a blot force
366 of 0 for 4-6 s prior to plunge freezing into liquid ethane. For the apo sample, two datasets
367 comprising of 804 and 1116 118-frame super-resolution movies each were collected with a 3x3
368 image shift at a magnification of 105,000x with physical pixel size of 0.834 Å/pix on a Titan Krios
369 (ThermoFisher) equipped with a K3 camera and a Bioquantum energy filter (Gatan) set to a slit
370 width of 20 eV. Collection dose rate was 8 $\text{e}^-/\text{pixel}/\text{second}$ for a total dose of 66 $\text{e}^-/\text{Å}^2$. Defocus
371 range was 0.8 to 2.4 μm . Each collection was performed with semi-automated scripts in
372 SerialEM. Nsp2 with Zn grids were prepared using a similar protocol. 1149 118-frame movies
373 were collected for this sample at a 105,000x magnification with physical pixel size of 0.834 Å/pix
374 on Titan Krios similar to without Zn sample. Collection dose rate was 8 $\text{e}^-/\text{pixel}/\text{second}$ for a total
375 dose of 67 $\text{e}^-/\text{Å}^2$.

376

377 **Data Processing**

378 **Without Zn:** Initial processing was done in Cryosparc (v2.15.0)¹⁷¹⁸. The first dataset with 801
379 dose-weighted motion corrected micrographs⁴⁴ was imported and Patch CTF(M) was
380 performed. This dataset required thorough manual curation and led to selection of 388
381 micrographs for further processing. Blob-picker was used to pick 363145 particles and
382 extraction was done with a box size of 288 px. 2D-classification was done into 150 classes and
383 good looking classes were selected with total 91181 particles. A second dataset with 1116
384 dose-weighted micrographs was processed in a similar manner. After Patch CTF(M), 748
385 micrographs were curated based on CTF-fit resolution (<5 Å), ice-thickness, and carbon.
386 Templates were created from the previous dataset and used for template-based particle picking
387 to get 577518 particles. 240551 particles were selected after 2D-classification into 200 classes.

388 These particles were merged with 91181 selected particles of the previous dataset after
389 2D-classification. Total 331732 particles were classified into 3 classes with heterogeneous
390 refinement. Multiple rounds of heterogeneous refinements, non-uniform refinements and
391 homogenous refinements resulted in a 3.45 Å 3D-reconstruction with 99076 particles. The
392 particles from this final step of Cryosparc processing were imported into Relion¹⁹ (version 3.0.8)
393 for further processing. 3D-classification without mask resulted in a 3.59 Å map. The core of the
394 map was better resolved therefore skip-align classification was done on the core. The best class
395 was subjected to 3D-refinement and post-processing leading to the final map at 3.49 Å. This
396 class was selected and skip-align classification was done for the full map. The overall resolution
397 of the full map with the selected 42579 particles was reported to be 3.76 Å which upon manual
398 inspection was the best looking map even though nominally being at worse resolution than
399 some previous reconstructions.

400

401 **With Zn:** Like the 'without Zn' dataset, for initial processing we used Cryosparc (v2.15.0). Patch
402 CTF(M) was performed on imported 1149 dose-weighted micrographs. The micrographs were
403 curated for CTF-fit resolution of better than 5 Å. Template-based particle picking was done
404 (templates from the without Zn dataset) on the selected 1028 micrographs, resulting in 1515264
405 particles. A series of ab-initio classifications followed by heterogeneous refinements and
406 non-uniform refinements on the best classes selected led to a map of 3.1 Å with 81817
407 particles. These particles were transferred to Relion (version 3.0.8) and a single-class skip-align
408 classification was performed with a mask. A 3.15 Å map with 81817 particles was obtained after
409 3D-refinement and post-processing on the particles from skip-align classification.

410

411 **Refinement/Model building**

412 The initial model for the core of 'without Zn' map was initially obtained by submitting the high
413 resolution region of the map with the full Nsp2 sequence to the DeepTracer server²⁰²¹. This

414 resulted in two chains which threaded the backbone fairly well but contained amino acid
415 substitutions/deletions. Therefore a homology model was built for Nsp2 using the resulting
416 model from DeepTrace server as a template, using SwissModel server. This model was then
417 refined against the map in Phenix Real Space Refine²⁴ and iteratively rebuilt with Rosetta
418 (2020.08 release)²⁵. Best scoring models were manually examined and corrected using COOT
419 0.9²². Rosetta was used for automatic iterative rebuilding the lower resolution regions of the map
420 and loops (212-224, 475-490). Cys/His residues were manually identified for Zn coordination
421 sites and Zn was placed in COOT. At this point the higher resolution cryo-EM map obtained in
422 the presence of zinc was used for downstream steps. Map/model quality was examined and
423 ramachandran outliers were fixed in ISOLDE 1.0²³. Rosetta FastRelax was used in cartesian
424 space followed by iterations of refinement in Phenix Real Space Refine. This fixed most of the
425 geometry outliers but introduced a large number of clashes in the model. Rosetta FastRelax in
426 torsion space was used on the model from Phenix Real Space Refine to resolve the clashes
427 while preserving good model statistics for the final model. The b-factors were assigned using
428 Rosetta B-factor fitting mover. Local resolution was determined by running ResMap program⁴⁵.
429 Directional FSC curves were determined by submitting the associated files to the 3DFSC
430 server⁴⁶.

431

432 **Obtaining full Nsp2 model incorporating AlphaFold2 prediction**

433 Predicted Nsp2 models were downloaded either from the DeepMind website or CASP14
434 website and then were aligned to the experimental Nsp2 map using matchmaker tool in
435 ChimeraX^{47,48}. Based on visual examination, the most updated (at the time of writing)
436 AlphaFold2 model (V3_4_8_2020) was split into 4 domains: 1-277, 278-344, 459-509 and
437 510-638. First three were individually aligned with matchmaker in ChimeraX to the experimental
438 model to assess the similarity and report RMSDs in the main text. These regions were not used
439 for downstream model building. The fourth region, 510-638 was rigid body fit into the 3.8 Å

440 cryo-EM map (obtained without zinc). The experimental model was then stitched together with
441 the rigid body fit domain for residues 510-638 from AlphaFold2. The whole model was energy
442 minimized into the cryo-EM density filtered to 5 Å by running Rosetta FastRelax in torsion
443 space.

444

445 **Sequence alignment and sequence conservation analysis**

446 Nsp2 sequences were manually downloaded from UniProt and aligned in Jalview using
447 MAFFT^{49,50}. Conservation was mapped on the Nsp2 structure using a combination of Chimera
448 and ChimeraX and the supplementary alignment figure was prepared with MView server^{47,51,52}.

449

450 **SARS-CoV-2 Nsp2 mammalian expression constructs.** SARS-CoV-2 isolate
451 2019-nCoV/USA-WA1/2020 (accession MN985325), an early-lineage sequence downloaded on
452 January 24, 2020, was the reference sequence for all viral expression constructs. Native
453 nucleotide sequences encoding proteolytically mature Nsp2 were first codon optimized
454 (<https://www.idtdna.com/codonopt>) for gene synthesis. The gBlock Gene Fragment (IDT)
455 encoding Nsp2 and the C-terminal linker and 2x-Strep tag was inserted into
456 pLVX-EF1alpha-IRES-Puro at the EcoRI and BamHI restriction sites by In-fusion cloning [PMID:
457 32353859]. SARS-CoV-2 Nsp2 mutants (D23Y/R27C, E63K/E66K, T85I, G262V/G265V, and
458 K330D/K337D) were generated in a similar manner using unique restriction sites within the
459 Nsp2 sequence to excise segments containing wild type residues. Sequences were
460 subsequently replaced by In-fusion cloning with gBlocks (IDT) containing mutated residues. All
461 mutations were confirmed by sequencing.

462

463 **Cell culture.** HEK293T cells were cultured in Dulbecco's Modified Eagle's Medium (Corning or
464 Gibco, Life Technologies) supplemented with 10% Fetal Bovine Serum (Gibco, Life

Technologies) and 1% Penicillin-Streptomycin (Corning) and maintained at 37°C in a humidified atmosphere of 5% CO₂.

Transfection. For each affinity purification (wild-type and mutant nsp2 and controls, empty vector and EGFP), 7.5 million HEK293T cells were plated per 15-cm dish and allowed to recover for 20-24 hours prior to transfection. Up to 15 µg of individual Strep-tagged expression constructs (normalized to 15 µg with empty vector as needed) was complexed with PolyJet Transfection Reagent (SignaGen Laboratories) at a 1:3 µg:µl ratio of plasmid to transfection reagent based on manufacturer's recommendations. After 40 hours, cells were dissociated at room temperature using 10 ml Dulbecco's Phosphate Buffered Saline without calcium and magnesium (D-PBS) supplemented with 10 mM EDTA for at least 5 minutes and subsequently washed with 10 ml D-PBS. Each step was followed by centrifugation at 200 xg, 4°C for 5 minutes. Cell pellets were frozen on dry ice and stored at - 80°C. At least three biological replicates were independently prepared for affinity purification.

Affinity purification. Frozen cell pellets were thawed on ice for 15-20 minutes and suspended in 1 ml Lysis Buffer [IP Buffer (50 mM Tris-HCl, pH 7.4 at 4°C, 150 mM NaCl, 1 mM EDTA) supplemented with 0.5% Nonidet P 40 Substitute (NP40; Fluka Analytical) and cOmplete mini EDTA-free protease and PhosSTOP phosphatase inhibitor cocktails (Roche)]. Samples were then frozen on dry ice for 10-20 minutes and partially thawed in a 37°C water bath. Following two freeze-thaw cycles, samples were incubated on a tube rotator for 30 minutes at 4°C and centrifuged at 13,000 xg, 4°C for 15 minutes to pellet debris. After reserving 50 µl lysate, samples were arrayed into a 96-well Deepwell plate for affinity purification on the KingFisher Flex Purification System (Thermo Scientific) as follows: MagStrep "type3" beads (30 µl; IBA Lifesciences) were equilibrated twice with 1 ml Wash Buffer (IP Buffer supplemented with 0.05%

NP40) and incubated with ~ 0.95 ml lysate for 2 hours. Beads were washed three times with 1 ml Wash Buffer, once with 1 ml IP Buffer and then transferred to 75 µl Denaturation-Reduction Buffer [2 M urea, 50 mM Tris-HCl pH 8.0, 1 mM DTT) aliquoted into 96-well plates for on-bead digestion (below)]. The KingFisher Flex Purification System was placed in the cold room and allowed to equilibrate to 4°C overnight before use. All automated protocol steps were performed using the slow mix speed and the following mix times: 30 seconds for equilibration/wash steps, 2 hours for binding, and 1 minute for final bead release. Three 10 second bead collection times were used between all steps.

On-bead digestion. Bead-bound proteins were incubated in Denaturation-Reduction Buffer for 30 minutes, alkylated in the dark with 3 mM iodoacetamide for 45 minutes and quenched with 3 mM DTT for 10 minutes. Proteins were then trypsin digested as follows: initially for 4 hours with 1.5 µl trypsin (0.5 µg/µl; Promega) and then another 2 hours with 0.5 µl additional trypsin. To offset evaporation during trypsin digestion, 22.5 µl 50 mM Tris-HCl, pH 8.0 was added. All steps were performed with constant shaking at 1,100 rpm on a ThermoMixer C incubator set to 37°C (denaturation-reduction and trypsin digest) or room temperature (alkylation and quenching). Digested peptides were combined with 50 µl 50 mM Tris-HCl, pH 8.0 used to backwash beads and acidified with trifluoroacetic acid (0.5% final, pH < 2.0) Acidified peptides were desalted using a BioPureSPE Mini 96-Well Plate (20mg PROTO 300 C18; The Nest Group, Inc.) according to standard protocols and dried in a CentriVap Concentrator (Labconco) for at least two hours.

Mass spectrometry data acquisition and analysis. Samples were re-suspended in 4% formic acid, 2% acetonitrile solution, and separated by a reversed-phase gradient over a nanoflow C18 column (Dr. Maisch). Each sample was directly injected via a Easy-nLC 1200 (Thermo Fisher Scientific) into a Q-Exactive Plus mass spectrometer (Thermo Fisher Scientific) and analyzed

515 with a 75 min acquisition, with all MS1 and MS2 spectra collected in the orbitrap; data were
516 acquired using the Thermo software Xcalibur (4.2.47) and Tune (2.11 QF1 Build 3006). For all
517 acquisitions, QCloud was used to control instrument longitudinal performance during the
518 project⁵³. All proteomic data was searched against the human proteome (uniprot reviewed
519 sequences downloaded February 28th, 2020), EGFP sequence, and the SARS-CoV-2 protein
520 sequences using the default settings for MaxQuant (version 1.6.12.0)^{54,55}. Detected peptides
521 and proteins were filtered to 1% false discovery rate in MaxQuant.

522 Identified proteins were then subjected to protein-protein interaction scoring with both
523 SAINTexpress (version 3.6.3)⁵⁶ and MiST (<https://github.com/kroganlab/mist>)^{57,58}. Interactions
524 passing the master threshold (MiST score ≥ 0.6 , a SAINTexpress BFDR ≤ 0.05 and an average
525 spectral count ≥ 2) for at least one of the baits (mutants or wild-types) were kept for further
526 analysis. An “Interaction Score” was defined as the average between the MiST score and the
527 Saint Score, as previously described¹⁰. In addition, interactions were removed if their detection
528 was found to be discrepant for wild-type Nsp2 between this study and a prior study² (difference
529 in interaction scores between studies < 0.4), further increasing the confidence of our final set of
530 interactions. Remaining interactions were separated into two groups: those interacting with
531 Nsp2 wild-type or not (average Interaction Score > 0.5 or < 0.5 were separated into Fig 5A-C
532 and Sup Fig 5A, respectively). For those interacting with wild-type, a quantitative statistical
533 analysis was performed (this quantitation was not possible for those not interacting with
534 wild-type Nsp2 due to the lack of detection). Specifically, prey intensities in each affinity
535 purification were normalized to the corresponding bait abundance using MSstats⁵⁹
536 (globalStandards norm). Log₂ fold changes and BH-adjusted p-values were calculated by
537 comparing each mutant to the wild-type from this study.

538 **Scheduled parallel reaction monitoring (PRM) analysis of Nsp2 interactors.** Peptides for
539 targeted MS were selected after importing the msms.txt file derived from the previously

described MaxQuant search into Skyline (v20.2.0.343)⁶⁰. Proteotypic peptides passing an Andromeda score of 0.95 were selected and manually inspected to choose precursors suitable for targeted proteomics. In total 4 peptides per protein were selected for targeted analysis. For WASHC4 and EIF4E2 all peptides identified by DDA were used (3 and 2 respectively). The samples from AP-MS were acquired in Partial Reaction Monitoring mode (PRM)⁶¹ on a Q-Exactive Orbitrap (Thermo Fisher) connected to a nanoLC easy 1200 (Thermo Fisher). Peptides for the scheduled analysis were separated in 75 minutes using the same chromatographic gradient and source parameter to the DDA samples. Precursor ion scans were recorded in the Orbitrap at 70'000 resolution (at 400 m/z) for 100 ms or until the ion population reached an AGC value of $1e^6$. Peptides in the inclusion list were fragmented using HCD with a normalized collisional energy of 27, an isolation window of 2 Da and a scheduled retention time window of 7 minutes. Fragments were acquired in the Orbitrap at 17'500 resolution (at 400 m/z) for 100 ms or until reaching an AGC of $2e^5$. Loop count was set to 20. For data analysis, the PRM data was searched with MaxQuant using a FASTA file containing only the target proteins and default settings. The msms.txt was imported into Skyline using the 'import peptide search' option and setting the search type to targeted. To import the files, the following transition settings were used: The MS1 filter was disabled, ion types were set to y and b and MS/MS settings were set to Orbitrap as mass analyzer, type as targeted and resolution of 17500 (at 400 m/z). Peptides with poor coeluting fragments (dotp lower than 0.9) were removed. WASHC4 peptides did not pass this quality control criterion and thus WASHC4 was not considered for further analysis. After import, peak boundaries were manually corrected and noisy transitions were removed. The resulting data was exported at the transition level and transitions missing in more than half of the samples were removed to ensure robust quantitation. The resulting transitions were summed up per peptide and then the experiment was mean centered using the average peptide level for the bait protein (using SARS-Cov-2 Nsp2 quantity for SARS-CoV-2 mutants). Normalized peptide-level abundances were averaged to reach protein level and \log_2

transformed. The fold change and BH-adjusted p-values for condition were calculated against the wild-type Nsp2.

Acknowledgments.

The authors acknowledge their partners and families for support in childcare and other matters during this time. We thank D. Mullins for helpful discussions and V. Ramani for providing critical feedback on the manuscript. The structural biology portion of this work was performed by the QCRG (Quantitative Biosciences Institute Coronavirus Research Group) Structural Biology Consortium. Listed below are the contributing members of the consortium listed by teams in order of team relevance to the published work. Within each team the team leads are italicized (responsible for organization of each team, and for the experimental design utilized within each team), then the rest of team members are listed alphabetically. **Bacterial expression team:** *Amy Diallo, Meghna Gupta, Erron W. Titus*, Jen Chen, Loan Doan, Sebastian Flores, Mingliang Jin, Huong T. Kratochvil, Victor L. Lam, Yang Li, Megan Lo, Gregory E. Merz, Joana Paulino, Aye C. Thwin, Zanlin Yu, Fengbo Zhou, Yang Zhang. **Protein purification team:** *Michelle Moritz, Tristan W. Owens, Sergei Pourmal*, Caleigh M. Azumaya, Cynthia M. Chio, Bryan Faust, Meghna Gupta, Kate Kim, Joana Paulino, Komal Ishwar Pawar, Jessica K. Peters, Kaitlin Schaefer, Ursula Schulze-Gahmen, Tsz Kin Martin Tsui. **CryoEM grid freezing/collection team:** *Caleigh M. Azumaya, Axel F. Brilot, Gregory E. Merz, Cristina Puchades, Alexandra N. Rizo, Ming Sun*, Julian R. Braxton, Meghna Gupta, Fei Li, Kyle E. Lopez, Arthur Melo, Gregory E. Merz, Frank R. Moss III, Joana Paulino, Thomas H. Pospiech, Jr., Sergei Pourmal, Amber M. Smith, Paul V. Thomas, Feng Wang, Zanlin Yu. **CryoEM data processing team:** *Axel F. Brilot, Miles Sasha Dickinson, Gregory E. Merz, Henry C. Nguyen, Alexandra N. Rizo*, Daniel Asarnow, Julian R. Braxton, Melody G. Campbell, Cynthia M. Chio, Un Seng Chio, Devan Diwanji, Bryan Faust, Soumya Govinda Remesh, Meghna Gupta, Nick Hoppe, Mingliang Jin, Fei Li, Junrui Li, Yanxin Liu, Adamo Mancino, Melissa Mendez, Joana Paulino, Thomas H. Pospiech, Jr., Sergei Pourmal, Smriti Sangwan, Raphael Trenker, Donovan

592 Trinidad, Eric Tse, Kaihua Zhang, Fengbo Zhou. **Mammalian cell expression team:** *Christian*
593 *Billesboelle, Melody G. Campbell, Devan Diwanji, Evelyn Hernandez, Carlos Nowotny, Amber*
594 *M. Smith, Jianhua Zhao, Caleigh M. Azumaya, Alisa Bowen, Nick Hoppe, Yen-Li Li, Edmond*
595 *Linossi, Jocelyne Lopez, Phuong Nguyen, Michael D. Paul, Cristina Puchades, Mali Safari,*
596 *Smriti Sangwan, Kaitlin Schaefer, Raphael Trenker, Tsz Kin Martin Tsui, Natalie Whitis.*
597 **Crystallography team:** *Nadia Herrera, Huong T. Kratochvil, Ursula Schulze-Gahmen, Iris D.*
598 *Young, Justin Biel, Ishan Deshpande, Xi Liu. Infrastructure team:* David Bulkley, Arceli Joves,
599 Almarie Joves, Liam McKay, Mariano C. Tabios, Eric Tse. **Leadership team:** *Oren S*
600 *Rosenberg, Kliment A Verba, David A Agard, Yifan Cheng, James S Fraser, Adam Frost,*
601 *Natalia Jura, Tanja Kortemme, Nevan J Krogan, Aashish Manglik, Daniel R. Southworth, Robert*
602 *M Stroud. The QCRG Structural Biology Consortium has received support from: Quantitative*
603 *Biosciences Institute, Defense Advance Research Projects Agency HR0011-19-2-0020 (to*
604 *D.A.A. and K.A.V.; B. Shoichet PI), FastGrants COVID19 grant (K.A.Verba PI), Laboratory For*
605 *Genomics Research (O.S. Rosenberg PI) and Laboratory For Genomics Research (R.M. Stroud*
606 *PI)*

607

608 **Author contribution statement.**

609 The following authors designed and generated protein constructs and also performed protein
610 expressions: M.G., A.D., G.E.M., D.C.D., E.H., V.L.L., Y.L., C.A.N., A.M.S., Z.Y., M.G.C., J.C.,
611 L.D., Y.L., E.L., M.L., J.L., M.D.P., M.S., A.C.T., E.W.T., R.T., Y.Z., J.Z.. The following authors
612 performed protein purifications: C.M.A., M.M., S.P., T.W.O., J.K.P., U.S.G., K.K., K.I.P., K.S.,
613 T.K.M.T., F.Z.. The following authors performed structural analysis (data collection by
614 crystallography or cryoEM and data processing and model building): M.G., C.M.A., S.P., G.E.M.,
615 A.F.B., N.H., H.T.K., F.L., H.C.N., A.N.R., I.D.Y., D.E.A., U.S.C., M.S.D., M.J., J.L., Y.L., K.E.L.,
616 A.M., F.R.M., T.H.P.Jr, C.P., S.G.R., M.S., E.T.. Graphene oxide grids were provided by F.W. and
617 Z.Y.. M.C.T. provided crucial infrastructural and organizational support. The following authors did

618 affinity purification mass spectrometry studies: G.M.J., M.B., A.F., K.C., A.P., Y.Z.. The following
619 authors supervised or managed research: D.A.A., Y.C., J.S.F., N.J., T.K., A.M., D.R.S., R.M.S.,
620 D.L.S., N.J.K., A.F., O.S.R., K.A.V.. The following authors designed and conceptualized the
621 study: M.G., C.M.A., M.M., S.P., A.D., G.E.M., M.B., L.Z.A., D.A.A., Y.C., J.S.F., N.J., T.K., A.M.,
622 D.R.S., R.M.S., N.J.K., A.F., O.S.R., K.A.V.. The following drafted the initial manuscript: M.G.,
623 M.M., S.P., G.E.M., G.M.J., M.B., A.F., F.L., L.Z.A., J.S.F., D.L.S., N.J.K., A.F., O.S.R., K.A.V.. All
624 authors edited the manuscript.

625

626 **Competing interests statement.**

627 J.S.F. is a founder of Keyhole Therapeutics and a shareholder of Relay Therapeutics and
628 Keyhole Therapeutics. The Fraser laboratory has received sponsored research support from
629 Relay Therapeutics. The Krogan Laboratory has received research support from Vir
630 Biotechnology and F. Hoffmann-La Roche. N.K. has consulting agreements with Maze
631 Therapeutics and Interline Therapeutics, and is a shareholder of Tenaya Therapeutics. A.F. is a
632 shareholder of Relay Therapeutics. A.F. has received sponsored research support from Relay
633 Therapeutics.

634

635 **Funding statement.**

636 This research was funded by: NIH NCI F32CA239333 to M.B.; NIH/NCI 1F30CA247147 to
637 D.C.D.; BWF 1019894 to N.H.; NIGMS K99GM138753 to H.T.K.; NIMH K99MH119591 to F.L.;
638 Damon Runyon Cancer Research Foundation postdoctoral award to T.W.O.; NIH
639 F32GM133084 to J.K.P.; NIH F32GM133129 to I.D.Y.; Alfred Benzon Foundation award to
640 C.B.B.; NIH NIGMS F32GM137463 to U.S.C.; American Heart Association #18POST33990362
641 to Y.L.; NIH T32EB9383 to K.E.L.; Damon Runyon Cancer Research Foundation postdoctoral
642 award to C.P.; Helen Hay Whitney Foundation to K.S.; DFG GZ: TR 1668/1-1 to R.T.; Human
643 Frontier Science Program (HFSP) fellowship to K.Z.; NSF RAPID 2031205 to J.S.F.; NIH GM

644 24485, AI095208, AI50476 to R.M.S.; FastGrants COVID-19 grant to K.A.V.; Laboratory For
645 Genomics Research grant to O.S.R. and R.M.S.; NIH (1R01AI128214, U19AI135990) to OSR;
646 NIH (P50AI150476, U19AI135990, U19AI135972, R01AI143292, R01AI120694, and
647 P01AI063302) to N.J.K; Excellence in Research Award (ERA) from the Laboratory for
648 Genomics Research (LGR), a collaboration between UCSF, UCB, and GSK (#133122P) to
649 N.J.K; Roddenberry Foundation to N.J.K; funding from F. Hoffmann-La Roche and Vir
650 Biotechnology and gifts from QCRG philanthropic donors. This work was supported by the
651 Defense Advanced Research Projects Agency (DARPA) under Cooperative Agreement
652 #HR0011-19-2-0020 (N.J.K, D.A.A., K.A.V.). The views, opinions, and/or findings contained in
653 this material are those of the authors and should not be interpreted as representing the official
654 views or policies of the Department of Defense or the U.S. Government. The UCSF Electron
655 Microscopy Facilities were partially funded by following grants: 1S10OD026881-01,
656 1S10RR026814-01, 1S10OD020054-01, 1S10OD021741-01.

657

658 **Data availability statement.**

659 The atomic coordinates and the associated cryoEM maps for both Nsp2 structures, with and
660 without zinc were deposited to the PDB and EMDB with PDB codes of XXXX and YYYY and
661 EMDB codes of XXXXX and YYYYYY. The mass spectrometry proteomics data have been
662 deposited to the ProteomeXchange Consortium via the PRIDE partner repository with the
663 dataset identifier PXD025817. Reviewers may access the dataset using the following
664 credentials: Username of reviewer_pxd025817@ebi.ac.uk and password of szYFYpXQ.

665

666

667 REFERENCES

- 668 1. V'kovski, P., Kratzel, A., Steiner, S., Stalder, H. & Thiel, V. Coronavirus biology and
669 replication: implications for SARS-CoV-2. *Nat. Rev. Microbiol.* (2020)
670 doi:10.1038/s41579-020-00468-6.
- 671 2. Gordon, D. E. *et al.* A SARS-CoV-2 protein interaction map reveals targets for drug
672 repurposing. *Nature* **583**, 459–468 (2020).
- 673 3. Thoms, M. *et al.* Structural basis for translational shutdown and immune evasion by the
674 Nsp1 protein of SARS-CoV-2. *Science* **369**, 1249–1255 (2020).
- 675 4. Miorin, L. *et al.* SARS-CoV-2 Orf6 hijacks Nup98 to block STAT nuclear import and
676 antagonize interferon signaling. *Proc. Natl. Acad. Sci. U. S. A.* **117**, 28344–28354 (2020).
- 677 5. García-Sastre, A. Ten Strategies of Interferon Evasion by Viruses. *Cell Host Microbe* **22**,
678 176–184 (2017).
- 679 6. Graham, R. L., Sims, A. C., Brockway, S. M., Baric, R. S. & Denison, M. R. The nsp2
680 replicase proteins of murine hepatitis virus and severe acute respiratory syndrome
681 coronavirus are dispensable for viral replication. *J. Virol.* **79**, 13399–13411 (2005).
- 682 7. Gadlage, M. J., Graham, R. L. & Denison, M. R. Murine coronaviruses encoding nsp2 at
683 different genomic loci have altered replication, protein expression, and localization. *J. Virol.*
684 **82**, 11964–11969 (2008).
- 685 8. Cornillez-Ty, C. T., Liao, L., Yates, J. R., 3rd, Kuhn, P. & Buchmeier, M. J. Severe acute
686 respiratory syndrome coronavirus nonstructural protein 2 interacts with a host protein
687 complex involved in mitochondrial biogenesis and intracellular signaling. *J. Virol.* **83**,
688 10314–10318 (2009).
- 689 9. von Brunn, A. *et al.* Analysis of intraviral protein-protein interactions of the SARS
690 coronavirus ORFeome. *PLoS One* **2**, e459 (2007).
- 691 10. Gordon, D. E. *et al.* Comparative host-coronavirus protein interaction networks reveal
692 pan-viral disease mechanisms. *Science* **370**, (2020).

- 693 11. Davies, J. P., Almasy, K. M., McDonald, E. F. & Plate, L. Comparative multiplexed
694 interactomics of SARS-CoV-2 and homologous coronavirus non-structural proteins
695 identifies unique and shared host-cell dependencies. *bioRxiv* (2020)
696 doi:10.1101/2020.07.13.201517.
- 697 12. V'kovski, P. *et al.* Determination of host proteins composing the microenvironment of
698 coronavirus replicase complexes by proximity-labeling. *Elife* **8**, (2019).
- 699 13. Zhao, J., Zhai, X. & Zhou, J. Snapshot of the evolution and mutation patterns of
700 SARS-CoV-2. *bioRxiv* (2020) doi:10.1101/2020.07.04.187435.
- 701 14. Deng, X. *et al.* Transmission, infectivity, and antibody neutralization of an emerging
702 SARS-CoV-2 variant in California carrying a L452R spike protein mutation.
703 doi:10.1101/2021.03.07.21252647.
- 704 15. Hodcroft, E. B. *et al.* Emergence in late 2020 of multiple lineages of SARS-CoV-2 Spike
705 protein variants affecting amino acid position 677. *medRxiv* (2021)
706 doi:10.1101/2021.02.12.21251658.
- 707 16. Hoffmann, H.-H. *et al.* Functional interrogation of a SARS-CoV-2 host protein interactome
708 identifies unique and shared coronavirus host factors. *Cell Host Microbe* (2020)
709 doi:10.1016/j.chom.2020.12.009.
- 710 17. Punjani, A., Rubinstein, J. L., Fleet, D. J. & Brubaker, M. A. cryoSPARC: algorithms for
711 rapid unsupervised cryo-EM structure determination. *Nat. Methods* **14**, 290–296 (2017).
- 712 18. Punjani, A., Zhang, H. & Fleet, D. J. Non-uniform refinement: adaptive regularization
713 improves single-particle cryo-EM reconstruction. *Nat. Methods* **17**, 1214–1221 (2020).
- 714 19. Zivanov, J. *et al.* New tools for automated high-resolution cryo-EM structure determination
715 in RELION-3. *Elife* **7**, (2018).
- 716 20. Pfab, J., Phan, N. M. & Si, D. DeepTracer for fast de novo cryo-EM protein structure
717 modeling and special studies on CoV-related complexes. *Proc. Natl. Acad. Sci. U. S. A.*
718 **118**, (2021).

- 719 21. Pfab, J. & Si, D. DeepTracer: Predicting Backbone Atomic Structure from High Resolution
720 Cryo-EM Density Maps of Protein Complexes. doi:10.1101/2020.02.12.946772.
- 721 22. Emsley, P., Lohkamp, B., Scott, W. G. & Cowtan, K. Features and development of Coot.
722 *Acta Crystallogr. D Biol. Crystallogr.* **66**, 486–501 (2010).
- 723 23. Croll, T. I. ISOLDE: a physically realistic environment for model building into low-resolution
724 electron-density maps. *Acta Crystallogr D Struct Biol* **74**, 519–530 (2018).
- 725 24. Liebschner, D. *et al.* Macromolecular structure determination using X-rays, neutrons and
726 electrons: recent developments in Phenix. *Acta Crystallogr D Struct Biol* **75**, 861–877
727 (2019).
- 728 25. Wang, R. Y.-R. *et al.* Automated structure refinement of macromolecular assemblies from
729 cryo-EM maps using Rosetta. *Elife* **5**, (2016).
- 730 26. Yu, K. *et al.* Purification, crystallization and preliminary X-ray analysis of nonstructural
731 protein 2 (nsp2) from avian infectious bronchitis virus. *Acta Crystallogr. Sect. F Struct. Biol.*
732 *Cryst. Commun.* **68**, 716–719 (2012).
- 733 27. Callaway, E. ‘It will change everything’: DeepMind’s AI makes gigantic leap in solving
734 protein structures. *Nature* vol. 588 203–204 (2020).
- 735 28. Computational predictions of protein structures associated with COVID-19.
736 [https://deepmind.com/research/open-source/computational-predictions-of-protein-structures](https://deepmind.com/research/open-source/computational-predictions-of-protein-structures-associated-with-COVID-19)
737 [-associated-with-COVID-19.](https://deepmind.com/research/open-source/computational-predictions-of-protein-structures-associated-with-COVID-19)
- 738 29. Hahn, S. & Roberts, S. The zinc ribbon domains of the general transcription factors TFIIIB
739 and Brf: conserved functional surfaces but different roles in transcription initiation. *Genes*
740 *Dev.* **14**, 719–730 (2000).
- 741 30. Hagemeijer, M. C. *et al.* Dynamics of Coronavirus Replication-Transcription Complexes.
742 *Journal of Virology* vol. 84 2134–2149 (2010).
- 743 31. Li, Z., Jaroszewski, L., Iyer, M., Sedova, M. & Godzik, A. FATCAT 2.0: towards a better
744 understanding of the structural diversity of proteins. *Nucleic Acids Res.* **48**, W60–W64

745 (2020).

746 32. Holm, L. DALI and the persistence of protein shape. *Protein Sci.* **29**, 128–140 (2020).

747 33. Dashboard. <http://covid19.datamonkey.org/>.

748 34. Hickey, K. L. *et al.* GIGYF2 and 4EHP Inhibit Translation Initiation of Defective Messenger
749 RNAs to Assist Ribosome-Associated Quality Control. *Mol. Cell* **79**, 950–962.e6 (2020).

750 35. Flower, T. G. & Hurley, J. H. Crystallographic molecular replacement using an in
751 silico-generated search model of SARS-CoV-2 ORF8. doi:10.1101/2021.01.05.425441.

752 36. Viklund, I.-M. *et al.* WAFL, a new protein involved in regulation of early endocytic transport
753 at the intersection of actin and microtubule dynamics. *Exp. Cell Res.* **315**, 1040–1052
754 (2009).

755 37. Derivery, E. *et al.* The Arp2/3 activator WASH controls the fission of endosomes through a
756 large multiprotein complex. *Dev. Cell* **17**, 712–723 (2009).

757 38. Carnell, M. *et al.* Actin polymerization driven by WASH causes V-ATPase retrieval and
758 vesicle neutralization before exocytosis. *J. Cell Biol.* **193**, 831–839 (2011).

759 39. Dilucca, M., Forcelloni, S., Georgakilas, A. G., Giansanti, A. & Pavlopoulou, A. Codon
760 Usage and Phenotypic Divergences of SARS-CoV-2 Genes. *Viruses* **12**, (2020).

761 40. Alonso, A. M. & Diambra, L. SARS-CoV-2 Codon Usage Bias Downregulates Host
762 Expressed Genes With Similar Codon Usage. *Front Cell Dev Biol* **8**, 831 (2020).

763 41. Tollenaere, M. A. X. *et al.* GIGYF1/2-Driven Cooperation between ZNF598 and TTP in
764 Posttranscriptional Regulation of Inflammatory Signaling. *Cell Rep.* **26**, 3511–3521.e4
765 (2019).

766 42. Simmonds, P. Rampant C→U Hypermethylation in the Genomes of SARS-CoV-2 and Other
767 Coronaviruses: Causes and Consequences for Their Short- and Long-Term Evolutionary
768 Trajectories. *mSphere* vol. 5 (2020).

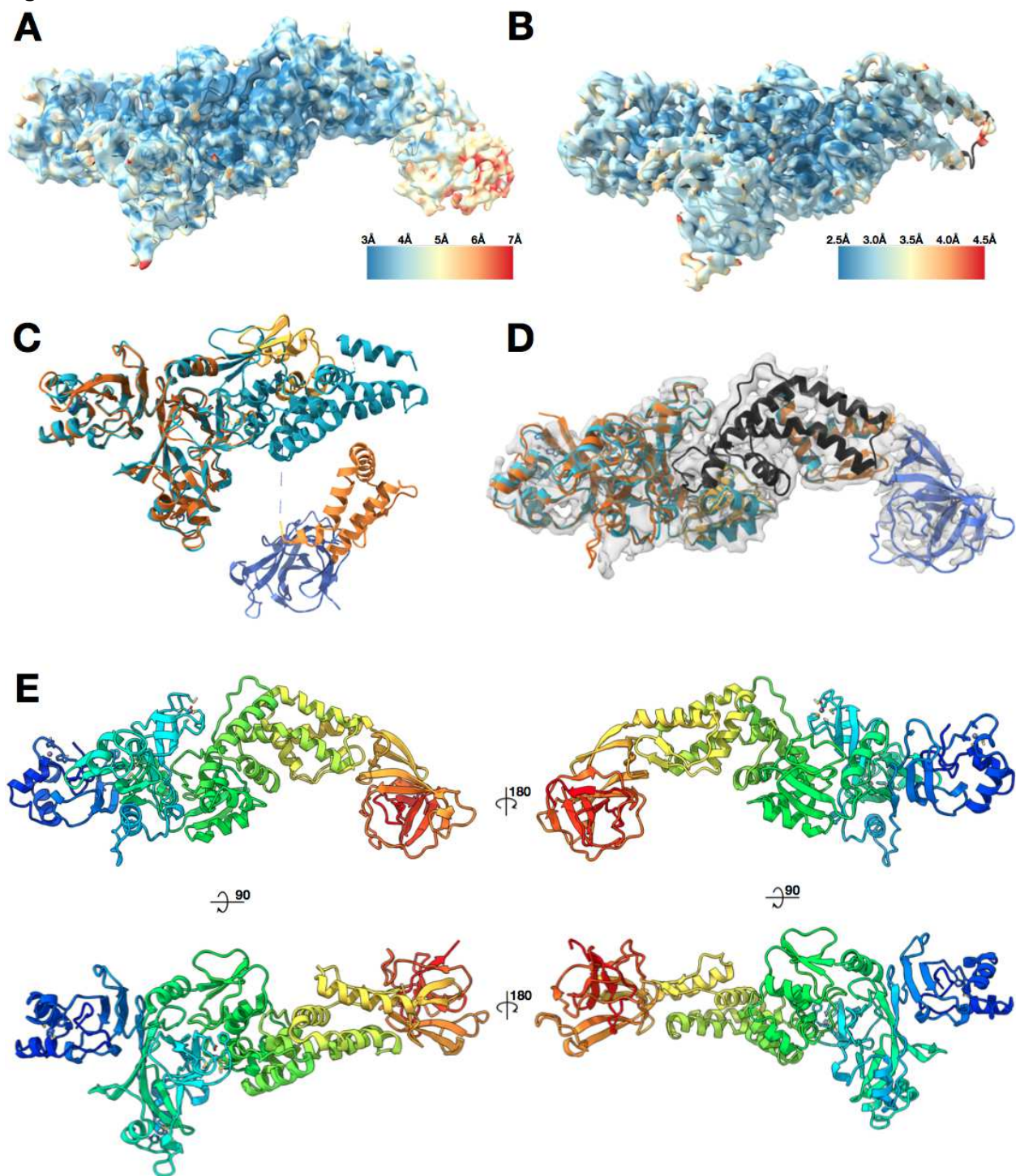
769 43. Pohl, M. O. *et al.* Distinct Phenotypes of SARS-CoV-2 Isolates Reveal Viral Traits Critical
770 for Replication in Primary Human Respiratory Cells. doi:10.1101/2020.10.22.350207.

- 771 44. Zheng, S. Q. *et al.* MotionCor2: anisotropic correction of beam-induced motion for improved
772 cryo-electron microscopy. *Nat. Methods* **14**, 331–332 (2017).
- 773 45. Kucukelbir, A., Sigworth, F. J. & Tagare, H. D. Quantifying the local resolution of cryo-EM
774 density maps. *Nat. Methods* **11**, 63–65 (2014).
- 775 46. Tan, Y. Z. *et al.* Addressing preferred specimen orientation in single-particle cryo-EM
776 through tilting. *Nat. Methods* **14**, 793–796 (2017).
- 777 47. Pettersen, E. F. *et al.* UCSF ChimeraX: Structure visualization for researchers, educators,
778 and developers. *Protein Sci.* **30**, 70–82 (2021).
- 779 48. Goddard, T. D. *et al.* UCSF ChimeraX: Meeting modern challenges in visualization and
780 analysis. *Protein Sci.* **27**, 14–25 (2018).
- 781 49. Waterhouse, A. M., Procter, J. B., Martin, D. M. A., Clamp, M. & Barton, G. J. Jalview
782 Version 2--a multiple sequence alignment editor and analysis workbench. *Bioinformatics* **25**,
783 1189–1191 (2009).
- 784 50. Katoh, K. & Standley, D. M. MAFFT multiple sequence alignment software version 7:
785 improvements in performance and usability. *Mol. Biol. Evol.* **30**, 772–780 (2013).
- 786 51. Pettersen, E. F. *et al.* UCSF Chimera--a visualization system for exploratory research and
787 analysis. *J. Comput. Chem.* **25**, 1605–1612 (2004).
- 788 52. Brown, N. P., Leroy, C. & Sander, C. MView: a web-compatible database search or multiple
789 alignment viewer. *Bioinformatics* vol. 14 380–381 (1998).
- 790 53. Chiva, C. *et al.* QCloud: A cloud-based quality control system for mass spectrometry-based
791 proteomics laboratories. *PLoS One* **13**, e0189209 (2018).
- 792 54. Cox, J. & Mann, M. MaxQuant enables high peptide identification rates, individualized
793 p.p.b.-range mass accuracies and proteome-wide protein quantification. *Nat. Biotechnol.*
794 **26**, 1367–1372 (2008).
- 795 55. Cox, J. *et al.* Accurate Proteome-wide Label-free Quantification by Delayed Normalization
796 and Maximal Peptide Ratio Extraction, Termed MaxLFQ. *Mol. Cell. Proteomics* **13**,

- 797 2513–2526 (2014).
- 798 56. Teo, G. *et al.* SAINTExpress: improvements and additional features in Significance Analysis
799 of INTERactome software. *J. Proteomics* **100**, 37–43 (2014).
- 800 57. Jäger, S. *et al.* Global landscape of HIV-human protein complexes. *Nature* **481**, 365–370
801 (2011).
- 802 58. Verschueren, E. *et al.* Scoring Large-Scale Affinity Purification Mass Spectrometry Datasets
803 with MiST. *Curr. Protoc. Bioinformatics* **49**, 8.19.1–16 (2015).
- 804 59. Choi, M. *et al.* MSstats: an R package for statistical analysis of quantitative mass
805 spectrometry-based proteomic experiments. *Bioinformatics* **30**, 2524–2526 (2014).
- 806 60. MacLean, B. *et al.* Skyline: an open source document editor for creating and analyzing
807 targeted proteomics experiments. *Bioinformatics* **26**, 966–968 (2010).
- 808 61. Peterson, A. C., Russell, J. D., Bailey, D. J., Westphall, M. S. & Coon, J. J. Parallel reaction
809 monitoring for high resolution and high mass accuracy quantitative, targeted proteomics.
810 *Mol. Cell. Proteomics* **11**, 1475–1488 (2012).

811
812
813

814 **Figure 1.**



816 **Figure 1. Nsp2 cryo-EM density and model overview.**

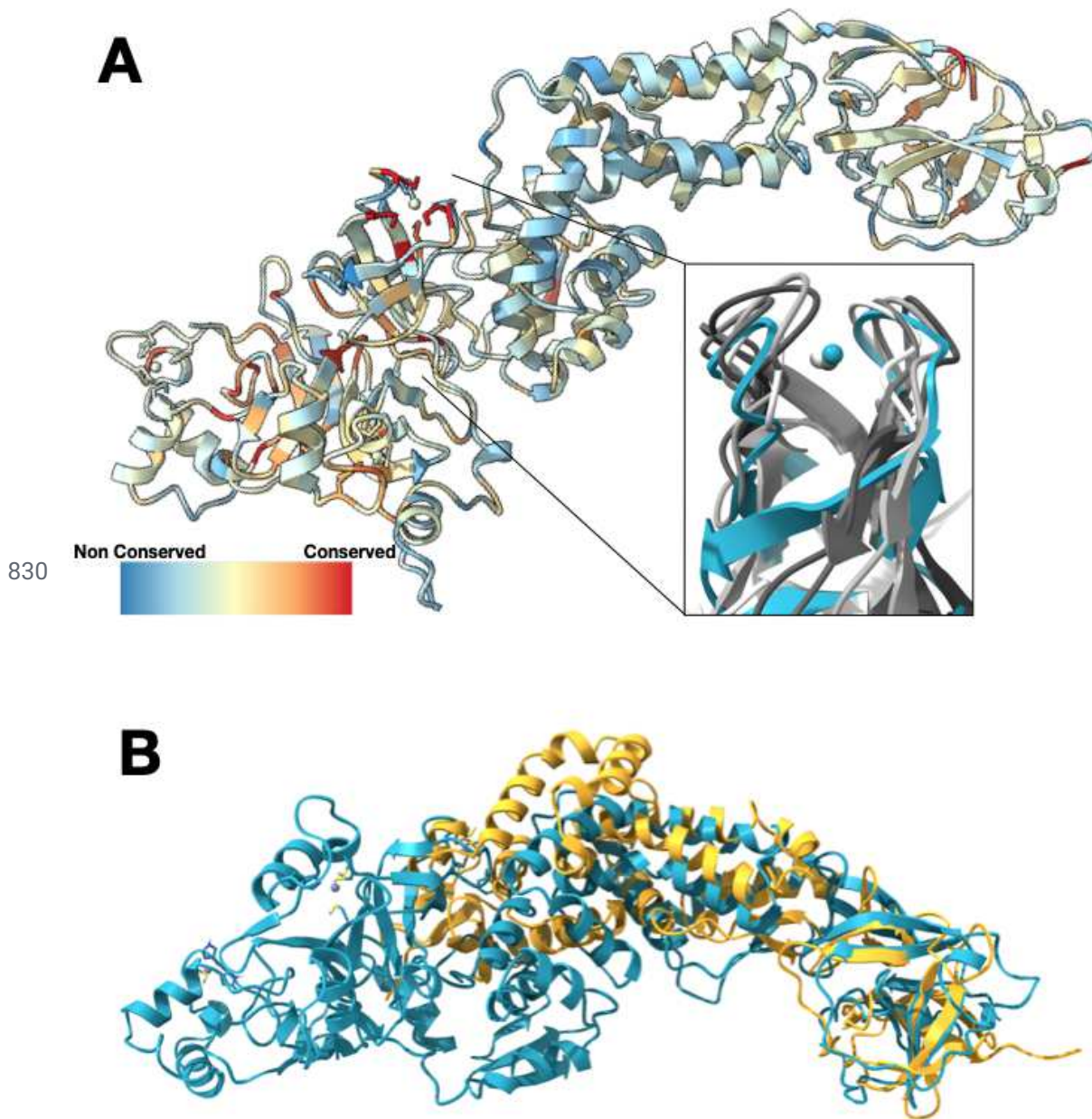
817 **(A)** 3.8 Å cryo-EM map of Nsp2 colored by local resolution showing the extra density at the

818 C-terminus **(B)** 3.2 Å cryo-EM map of Nsp2 colored by local resolution with the resulting model

819 in ribbon **(C)** Most up to date AlphaFold2 Nsp2 model (multicolored) was aligned to the
820 experimentally built Nsp2 model shown in cyan ribbon. The missing 93 amino acids from the
821 latest AlphaFold2 prediction are indicated by a dashed line. **(D)** AlphaFold2 Nsp2 predicted
822 model (same as **C**) was broken into 4 regions and then individually aligned to the experimentally
823 built model (domains segmented from the AlphaFold2 prediction are in shades of orange,
824 experimental model is in cyan, in black is the region missing from the AlphaFold2 prediction but
825 built into the experimental model, in blue is the C-terminal domain as predicted by AlphaFold2
826 and fit into the 3.8 Å cryo-EM map) (E) The resulting full length Nsp2 structure depicted as
827 ribbon and colored as rainbow, blue for N terminus to red for C-terminus.

828

829 **Figure 2.**



831

832 **Figure 2. Nsp2 has a conserved zinc binding motif but otherwise shows low**
833 **conservation.**

834 **(A)** Nsp2 structure depicted as ribbon and colored by conservation (see methods for details).

835 The four cysteines show the highest conservation and are indicated in red. The magnified insert

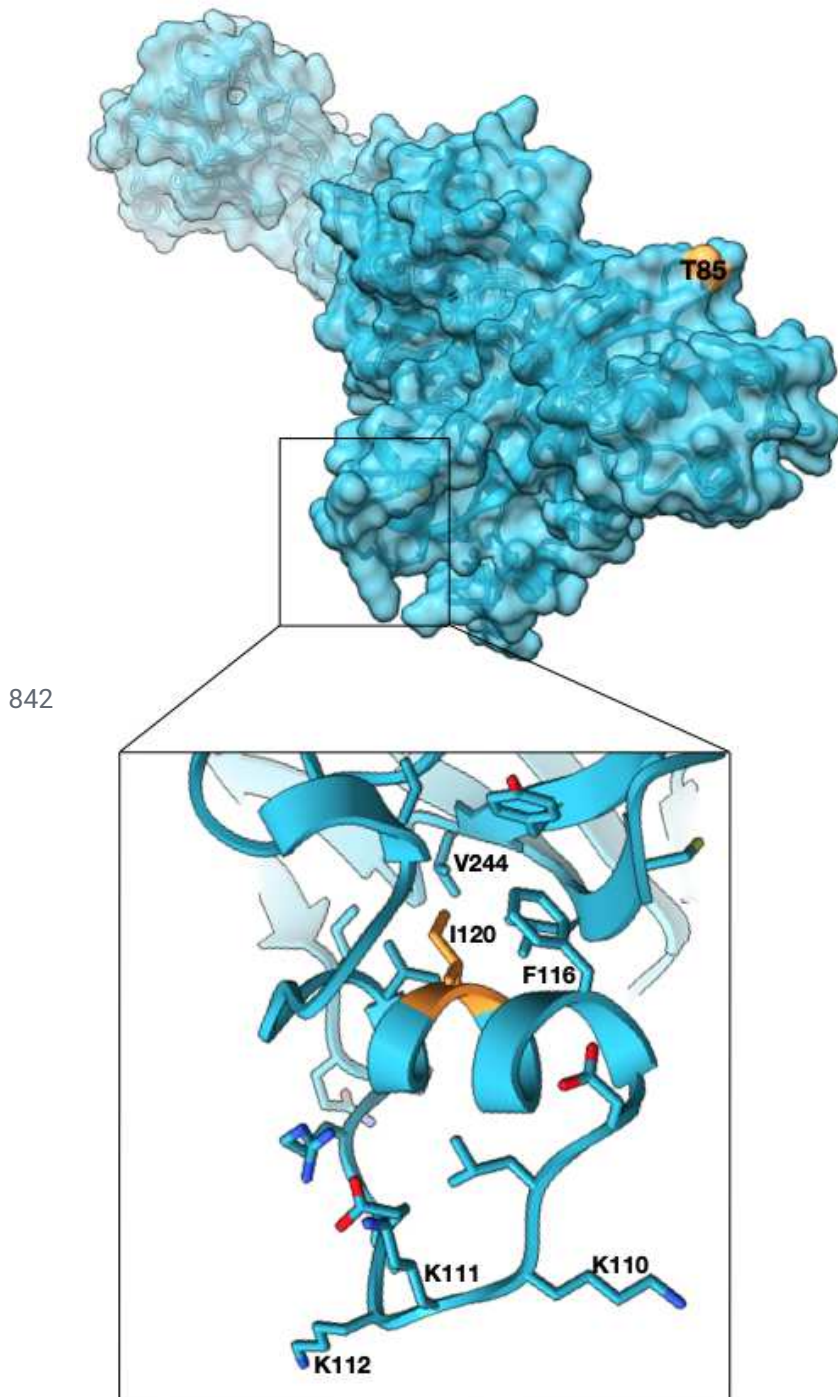
836 shows the zinc ribbon motif of Nsp2 in cyan aligned to zinc ribbon motifs from structurally similar

837 structures in the PDB in shades of gray (PDBs: 1JJ2, 5XON, 1QUP, 4C2M). **(B)** Structure of IBV

838 Nsp2 (PDB:3LD1, yellow ribbon) aligns well to the C-terminal region of SARS-CoV-2 Nsp2
839 (cyan) even though it has less than 10% sequence identity.

840

841 **Figure 3.**



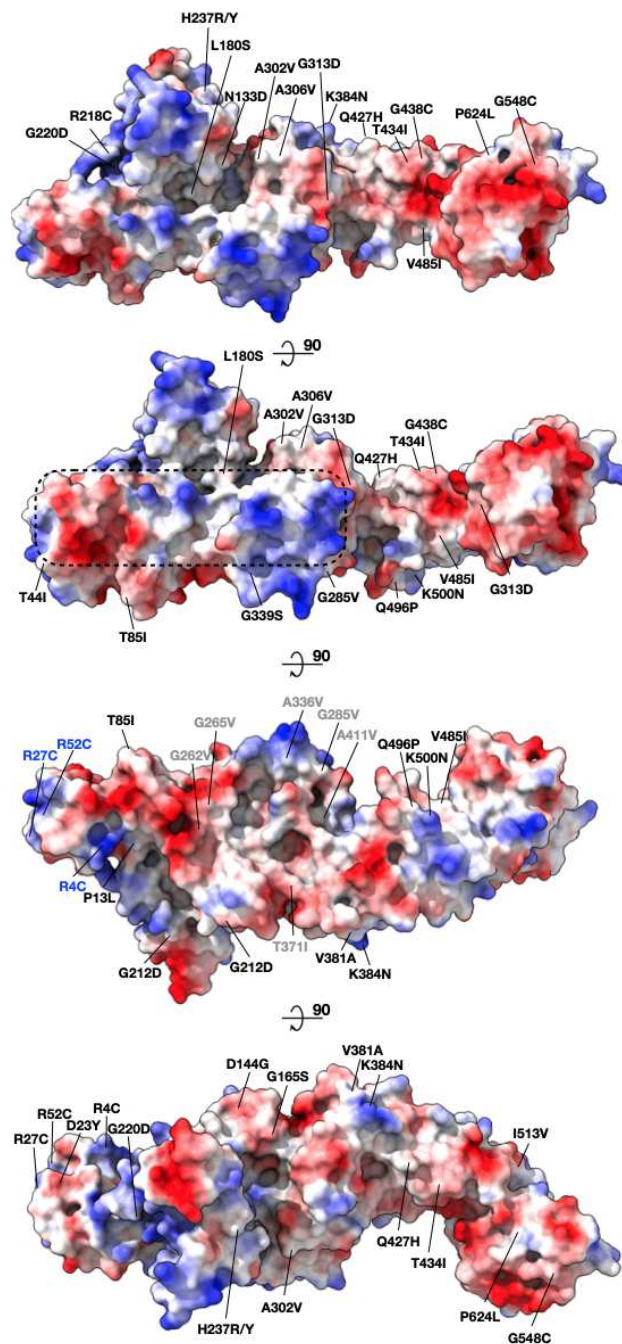
843 **Figure 3. High frequency mutations in Nsp2 may provide host specific advantages.**

844 T85I mutation which is present in 13% of all the SARS-CoV-2 sequences is at the surface and
845 may mediate host specific protein-protein interactions (Nsp2 surface in cyan, T85 in orange).
846 Another mutated site, I120 points into a hydrophobic core stabilizing a small helix which is

847 attached to a highly positively charged surface loop. Phe substitution at the site may further
848 stabilize the helix. (zoomed panel, I120 in orange).

849

850 **Figure 4.**



852

853 **Figure 4. Mapping surface mutations in SARS-CoV-2 Nsp2 shows both potentially**
 854 **constrained surfaces and rapidly changing regions.**

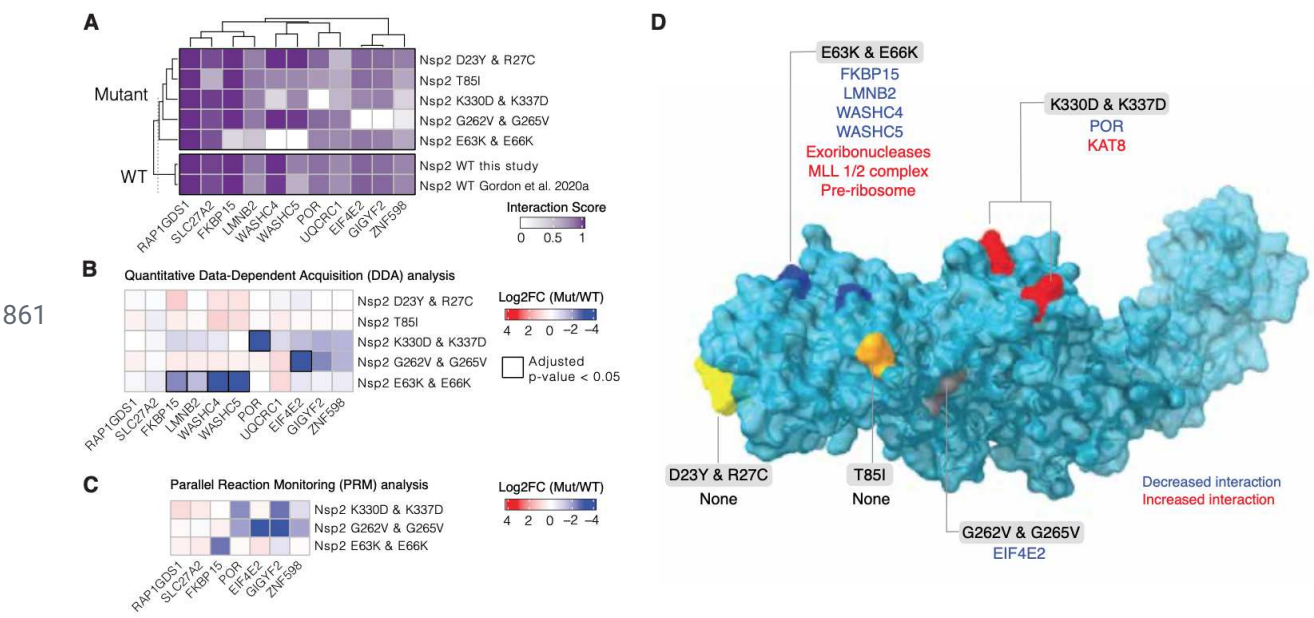
855 All the positively selected mutations on Nsp2 mapped to the protein surface are colored by the
 856 surface charge. The region that is less susceptible to mutations is inscribed in a dashed

857 rectangle. Residues that became less charged at the N-terminus are marked in blue (cluster 1).

858 Residues that became more hydrophobic are marked in gray (cluster 2).

859

860 **Figure 5.**



862 **Figure 5. Nsp2 possesses multiple interaction surfaces for host proteins.**

863 **(A)** Interaction scores (average between MiST and Saint Scores) for human proteins (“preys”) 864 deemed high-confidence interactions in at least one affinity purification (“bait”) mass 865 spectrometry assay and detected to interact with both the wild-type Nsp2 in this study and in 866 Gordon et al (2020a). Interaction scores range from zero to one, one being the most 867 high-confidence. **(B)** Quantitative statistical analysis of data-dependent acquisition (DDA) mass 868 spectrometry data using MSstats for interactions selected and depicted in **A**. Prey intensities 869 were normalized by bait expression abundance. Log₂ fold changes and BH-adjusted p-values 870 were calculated by comparing each mutant to the wild-type from this study. Square black 871 outlines depict adjusted p-values < 0.05. **(C)** Parallel reaction monitoring (PRM) analysis of 872 select preys from B for mutants found to possess significantly-changed interactions (adjusted 873 p-value < 0.05). **(D)** Nsp2 structure depicted as surface (light blue) with the mutations 874 considered in this study depicted on the surface: E63K/E66K (dark blue), K330D/K337D (red), 875 D23Y/R27C (yellow), T85I (orange), and G262V/G265V (grey). Lost interactions (adjusted 876 p-value < 0.05) from data-dependent acquisition global proteomics analysis (DDA) from B 877 depicted in blue and gained protein complexes depicted in red (see Sup Fig 4)

Supplementary Files

This is a list of supplementary files associated with this preprint. Click to download.

- [D1000254629valreportfullP1.pdf](#)
- [D1000253535valreportfullP1.pdf](#)
- [SupplementaryFiles.pdf](#)
- [nreditorialpolicychecklistKVfilled.pdf](#)
- [TableS2.xlsx](#)